Imaging the impact of single oxygen atoms on superconducting $Bi_{2+y}Sr_{2-y}CaCu_2O_{8+x}$

Ilija Zeljkovic[(1)], *Zhijun Xu*[(2)], *Jinsheng Wen*[(2)], *Genda Gu*[(2)], *Robert S. Markiewicz*[(3)],
Jennifer E. Hoffman[(1),*]

(1) Department of Physics, Harvard University, 17 Oxford St., Cambridge, MA 02138, U.S.A.
(2) Condensed Matter Physics & Materials Science Department, Brookhaven National Laboratory, Upton, NY 11973-5000, U.S.A.
(3) Department of Physics, Northeastern University, 360 Huntington Ave., Boston, MA 02115, U.S.A.
* To whom correspondence should be addressed: jhoffman@physics.harvard.edu

High temperature cuprate superconductors display surprising nanoscale inhomogeneity in essential properties such as pseudogap energy, Fermi surface, and even superconducting critical temperature. Theoretical explanations for this inhomogeneity have ranged from chemical disorder to spontaneous electronic phase separation. We extend the energy range of scanning tunneling spectroscopy on $Bi_{2+y}Sr_{2-y}CaCu_2O_{8+x}$, allowing a complete mapping of two types of interstitial oxygen dopants and vacancies at the apical oxygen site. We show that the nanoscale spatial variations in the pseudogap states are correlated with disorder in these dopant concentrations, particularly that of apical oxygen vacancies.

Many of today's prominent materials, such as high-T_c superconductors, doped semiconductors, and colossal magnetoresistance materials, are non-stoichiometric and electronically inhomogeneous at the nanoscale (*1*). Both desirable and undesirable electronic properties may arise from chemical inhomogeneity. To fully understand and harness these materials, and to drive the discovery of new materials, it is crucial to understand the impact of single atoms on these inhomogeneous electronic states.

Cuprate superconductors are quasi-2D materials that arise from off-stoichiometric doping of a Mott insulator by oxygen intercalation and/or cation substitution. Nanoscale electronic inhomogeneity in the cuprates has been predicted (*2,3*) and detected (*4-7*), but the role of spontaneous electronic phase separation (*2*) and chemical disorder (*3*) is unresolved. Scanning tunneling microscopy (STM) has thus far lacked the necessary energy range to image the full set of relevant dopants. We present atomically resolved STM spectroscopy on $Bi_{2+y}Sr_{2-y}CaCu_2O_{8+x}$ (BSCCO) which doubles the energy range of previous work (*8*) and demonstrates the impact of single dopant atoms on electronic states.

In BSCCO, a prominent gap in the density of states shows energy variation of ~100%, on a 2-3nm length scale, across a wide range of doping (*9*). Recent studies (*10,11*) suggest that this spectral inhomogeneity results primarily from variations in the pseudogap (PG), a depression in the density of states near the Fermi level ε_F which persists far above the superconducting transition temperature T_c, most dominantly on the underdoped side of the phase diagram. Nanoscale variation in the PG offers the opportunity to uncover the variable(s) determining its local strength, thus setting the stage for control of this mysterious phase, whose energy scale anti-correlates with superconductivity (*12,13*), and which many believe is a competitor to superconductivity (*11,14*).

Several previous studies searched for chemical origins of spectral gap variation in BSCCO. Kinoda *et al* observed atomic defects in Pb-doped BSCCO with resonance energy +1.7 eV, identified as Bi^{3+} substitutions at the Sr^{2+} site (*15*). These defects may correlate weakly with regions of large PG, but no quantitative analysis was presented (*16*). McElroy *et al* observed localized conductance signatures in BSCCO at -0.96V, identified as interstitial oxygen dopants (*8*), but several mysteries were left unresolved. First, the counted oxygen fell ~50% short of the expected density for each T_c (*17*). Second, the correlation between oxygen locations and PG was weak and of unexpected sign: although it is well-established that globally increasing oxygen content correlates with decreasing PG (*12,13*), McElroy found that the oxygen dopant locations were weakly correlated with regions of increased gap.

To resolve the latter issue, one carefully tuned theory suggested that the dominant local effect of interstitial oxygens may be strain, which increases the local pairing strength (*18,19*). A second proposal by Zhou *et al* (*20*) explained both the missing oxygen and the counterintuitive correlation by postulating the existence of two types of interstitial oxygen dopants: 'type-B' oxygens observed by McElroy, which live around the BiO plane and contribute only delocalized charge, and 'type-A' which live around the SrO plane, and have an immediate electrostatic effect, locally hole doping the adjacent CuO_2 layer. Therefore, Zhou *et al* predicted that the type-A oxygens would follow the expected global trend: a strong anti-correlation with the PG. The weak correlation observed between McElroy's type-B oxygens and the PG could be explained as a side effect of slight repulsion between type-B and type-A oxygens. (See additional discussion in Supplementary Materials (SM), section I.) However, the type-A oxygens were predicted to have resonances even farther below ε_F than the -0.96V type-B's. This experimental challenge has prevented their observation to date.

We set out to observe the high energy dopants and elucidate their role in cuprate inhomogeneity. BSCCO was grown via floating zone technique. As is common to facilitate the growth process, the starting composition for all crystals studied here contained Bi:Sr in a ratio 2.1:1.9. By some combination of cation substitution and oxygen intercalation, as-grown crystals tended to be optimally doped with T_c~91K. Some samples were then annealed at 550°C in vacuum to remove oxygen and reduce T_c towards the underdoped side of the phase diagram. We present STM data from four samples with decreasing oxygen content and T_c=91K, 82K, 68K, and 55K. The samples were cleaved in cryogenic ultra-high-vacuum, and immediately inserted into our home-built STM, where they were imaged at T=6K.

Fig. 1A shows a topography of the BiO surface of BSCCO with T_c=55K, demonstrating atomic resolution at +1V bias. Fig. 1B shows the local differential tunneling conductance $g(\vec{r}, V = -1\mathrm{V})$, approximately proportional to the local density of states at -1 eV, acquired over the same area as Fig. 1A, containing atomic scale features of similar form and concentration to the previously observed type-B oxygen dopants (*8*). Fig. 1C extends the energy range down to show $g(\vec{r}, V = -1.5\mathrm{V})$, resolving a second set of atomic scale features presumed to be the predicted type-A interstitial oxygen dopants (*20*). Fig. 1D extends the energy range up to show $g(\vec{r}, V = +1\mathrm{V})$, revealing a third set of atomic-scale features. We observe no other distinct atomic-scale features in $g(\vec{r}, V)$ images at biases between -2V and +1.6V.

To clarify the identity of these 3 features, we repeat the same measurements on four different samples, and show the density of each type of dopant vs. T_c in Fig. 1E. As expected, we observe a monotonic decrease in the number of both types of interstitial oxygen dopants with falling T_c. However, the +1V features increase from virtually zero for optimally doped BSCCO, to almost 1% per CuO_2 plaquette for the T_c=55K sample. Previous studies detected no change in cation concentration on annealing up to 840°C (*21*), so our observed increasing concentration after 550°C vacuum annealing suggests instead oxygen site vacancies. There are 3 distinct oxygen lattice sites, but because the +1V features are laterally aligned with the Bi site, we identify them as missing apical oxygen atoms in the SrO layer (figs. S1-S3 and accompanying text).

Typical differential conductance spectra at each of the 3 types of dopants, and the background are shown in Fig. 1F. The defining features used to identify the impurities, such as the peak around -1V for a type-B oxygen, and the sudden changes of the slope around -1.2V and +0.8V for type-A oxygen and apical oxygen vacancy respectively, are robust for different setup condition, location, and sample (fig. S4).

We investigate the relationship of these dopants to the inhomogeneous PG. Fig. 2, A-C show the three types of dopants (two interstitials and one vacancy), superimposed on a PG map acquired for a BSCCO sample with T_c=55K (see figs. S5-S7 accompanying text for details of PG determination). Any correlation between type-B oxygens and PG is too weak to be seen by the naked eye. In contrast to Zhou's prediction, the type-A oxygens are correlated with regions of large PG. One immediately sees the strongest correlation between apical oxygen vacancies and PG. Fig. 2D shows the cross-correlations between the positions of the dopant atoms and the corresponding gapmap. Fig. 2E shows the average PG as a function of distance from the nearest dopant. This behavior is consistent across the three underdoped samples studied (figs. S8 and S9).

We examine more carefully the surprising departure from Zhou's prediction in Fig. 3, which plots the local PG energy vs. the local concentration of each dopant type. For the type-B interstitial oxygens in Fig 3A, the local trend within each sample shows correlation between increased local oxygen concentration and increased local PG; the global trend between samples shows anti-correlation between global oxygen concentration and global PG. In contrast to Zhou's prediction, Fig. 3B shows that a qualitatively similar juxtaposition of local and global trends holds for the type-A interstitial oxygens in the three underdoped samples. However, Fig. 3C shows excellent alignment of local and global trends for the correlation between apical oxygen vacancy density and PG. This suggests that in underdoped samples, variations in the local hole concentration, and thus the local PG, are governed primarily by the local removal of holes by apical oxygen vacancies, rather than the strain or the donation of localized holes from the interstitial oxygens.

The interstitial oxygens, previously predicted (*3*) to determine the local gap, do contribute delocalized holes, but in underdoped samples even the type-A interstitial oxygen positions remain correlated to regions of decreased local hole concentration, likely due to a tendency to remain close to the apical oxygen vacancies. In the optimally doped sample, the apical oxygen vacancy concentration is negligible, so the local hole concentration may be set by the next closest dopant to the CuO_2 plane, the type-A interstitial oxygen, as predicted by Zhou *et al* (*20*). Indeed Fig 3B shows that the local PG decreases with increasing local type-A concentration in the T_c=91K sample. We therefore reconcile the apparent contradiction between the global (*12,13*) and local (*7,8*) doping trends for both types of interstitial oxygens.

Does dopant inhomogeneity cause PG inhomogeneity or merely pin intrinsic inhomogeneity, caused perhaps by strong correlations? Because the 2-3nm length scale of PG inhomogeneity remains the same across a wide range of dopant concentrations (fig. S7A, inset), intrinsic PG inhomogeneity seems plausible. However, our experiment shows clearly that the dopant locations which are fixed at high T, particularly the apical oxygen vacancies, do govern the local PG strength which is subsequently determined on cooling through T*.

Our experiment measures directly the strong correlation between apical oxygen vacancies and the PG, but is there a relationship between apical oxygens and superconductivity itself? In fact, apical oxygen effects may be credited for the discovery of high-T_c superconductivity, as Müller was originally driven to explore the LaBaCuO system by the expectation of strong electron-phonon coupling due to the Jahn-Teller effect in the CuO_6 octahedral environment, specifically the displacement of the Cu-apical-O bond (*22*). However, subsequent isotope effect measurements suggested that any phonon contribution to superconductivity is dominated by CuO_2 plane oxygen (*23*). We conjecture that the apical oxygen vacancies influence the superconductivity indirectly in underdoped samples: by reducing the local hole concentration, which locally strengthens the PG, tying up antinodal states (*11,14*) and locally decreasing the Fermi level carriers which would otherwise be available for coherent pairing. Calculations also showed a correlation between T_c and apical oxygen height, and emphasize the importance of the axial orbital for the hopping and phase coherence necessary for superconductivity (*24,25*). Thus apical oxygen vacancies may lower the local superconducting T_c and/or critical current J_c.

Another manifestation of electronic inhomogeneity is a disordered ‘checkerboard’ (CB) modulation of the spectral weight which is static but most noticeable at energies within and near the PG energy. Field (*26*), doping (*9*), and temperature (*27*) dependence suggest that the CB is in fact the electronic ordered phase associated with the PG. The CB wavevector tracks the antinodal nesting wavevector across a wide range of doping (*28*). A closely related disordered periodic inhomogeneity arises from elastic scattering between degenerate states; this dispersing quasiparticle interference (QPI) may exist at similar wavevectors to the static CB, but only at a limited range of energies within the superconducting gap (*29*).

It was previously claimed that type-B oxygen dopants are found in the minima of the QPI patterns (*8*), at both positive and negative energies. However, QPI has opposite spatial phase for filled and empty states (*30*), suggesting that the previously observed correlation (*8*) relates instead to the CB. Fig. 4A shows the distribution of the three types of observed atomic dopants on top of a filtered $g(\vec{r}, V = 36\mathrm{mV})$ image (fig. S10-S12). A histogram of the distance from each dopant to the center of the nearest ‘checker’ (Fig. 4B) demonstrates the strong tendency of apical oxygen vacancies to lie in the peaks of the imaged CB, and weaker tendency for interstitial oxygen dopants to lie in the troughs. We therefore conclude that the apical oxygen vacancies play the primary role in pinning the CB.

Our high bias atomically resolved STS results suggest a possible route to increase T_c in BSCCO: underdope to increase the pairing potential (*31*), but explore different annealing recipes to allow interstitial oxygen removal without creating apical oxygen vacancies – the defects most favorable to the PG and possibly competitive to superconductivity. Recently, a ~15% increase in maximum T_c has been predicted from alternate dopant arrangements (*32*). Our spectroscopy methods may also prove useful in future studies of the effects of single atom impurities in other fragile quasi-2D materials.

References and Notes

1. E. Dagotto, Complexity in strongly correlated electronic systems. *Science* **309**, 257 (2005).

2. V. J. Emery, S. A. Kivelson, O. Zachar, Spin-gap proximity effect mechanism of high-temperature superconductivity. *Physical Review B* **56**, 6120 (1997).

3. I. Martin, A. Balatsky, Doping-induced inhomogeneity in high-T_c superconductors, *Physica C* **357-360**, 46 (2001).

4. S.-H. Pan *et al.*, Microscopic electronic inhomogeneity in the high-T_c superconductor $Bi_2Sr_2CaCu_2O_{8+x}$. *Nature* **413**, 282 (2001).

5. K. M. Lang *et al.*, Imaging the granular structure of high-T_c superconductivity in underdoped $Bi_2Sr_2CaCu_2O_{8+\delta}$. *Nature* **415**, 412 (2002).

6. K. K. Gomes *et al.*, Visualizing pair formation on the atomic scale in the high-T_c superconductor $Bi_2Sr_2CaCu_2O_{8+\delta}$. *Nature* **447**, 569 (2007).

7. W. D. Wise *et al.*, Imaging nanoscale Fermi-surface variations in an inhomogeneous superconductor. *Nature Physics* **5**, 213 (2009).

8. K. McElroy *et al.*, Atomic-Scale Sources and Mechanism of Nanoscale Electronic Disorder in $Bi_2Sr_2CaCu_2O_{8+\delta}$. *Science* **309**, 1048 (2005).

9. K. McElroy *et al.*, Coincidence of Checkerboard Charge Order and Antinodal State Decoherence in Strongly Underdoped Superconducting $Bi_2Sr_2CaCu_2O_{8+\delta}$. *Physical Review Letters* **94**, 197005 (2005).

10. M. C. Boyer *et al.*, Imaging the two gaps of the high-temperature superconductor $Bi_2Sr_2CuO_{6+x}$. *Nature Physics* **3**, 802 (2007).

11. A. Pushp *et al.*, Extending universal nodal excitations optimizes superconductivity in $Bi_2Sr_2CaCu_2O_{8+\delta}$. *Science* **324**, 1689 (2009).

12. G. Deutscher, Coherence and single-particle excitations in the high-temperature superconductors. *Nature* **397**, 410 (1999).

13. S. Hüfner, M. A. Hossain, A. Damascelli, G. A. Sawatzky, Two gaps make a high-temperature superconductor? *Reports on Progress in Physics* **71**, 062501 (2008).

14. T. Kondo, R. Khasanov, T. Takeuchi, J. Schmalian, A. Kaminski, Competition between the pseudogap and superconductivity in the high-T_c copper oxides. *Nature* **457**, 296 (2009).

15. G. Kinoda *et al.*, Direct determination of localized impurity levels located in the blocking layers of $Bi_2Sr_2CaCu_2O_y$ using scanning tunneling microscopy/spectroscopy, *Physical Review B* **71**, 020502 (2005).

16. G. Kinoda, T. Hasegawa, Observations of electronic inhomogeneity in heavily Pb-doped $Bi_2Sr_2CaCu_2O_y$ single crystals by scanning tunneling microscopy. *Physical Review B* **67**, 224509 (2003).

17. M. Presland, J. Tallon, R. Buckley, R. Liu, N. Flower, General trends in oxygen stoichiometry effects on T_c in Bi and Tl superconductors. *Physica C* **176**, 95 (1991).

18. T. Nunner, B. Andersen, A. Melikyan, P. Hirschfeld, Dopant-Modulated Pair Interaction in Cuprate Superconductors. *Physical Review Letters* **95**, 177003 (2005).

19. W. Chen, M. Gabay, P. J. Hirschfeld, Doping dependence of gap inhomogeneities at $Bi_2Sr_2CaCu_2O_{8+\delta}$ surfaces. *New Journal of Physics* **14**, 033004 (2012).

20. S. Zhou, H. Ding, Z. Wang, Correlating Off-Stoichiometric Doping and Nanoscale Electronic Inhomogeneity in the High-T_c Superconductor $Bi_2Sr_2CaCu_2O_{8+\delta}$. *Physical Review Letters* **98**, 076401 (2007).

21. D. Mitzi, L. Lombardo, A. Kapitulnik, S. Laderman, R. Jacowitz, Growth and properties of oxygen- and ion-doped $Bi_2Sr_2CaCu_2O_{8+\delta}$ single crystals. *Physical Review B* **41**, 6564 (1990).

22. J. G. Bednorz, K. A. Muller, Possible high T_c superconductivity in the Ba-La-Cu-O system. *Zeitschrift für Physik B* **64**, 189 (1986).

23. D. Zech *et al.*, Site-selective oxygen isotope effect in optimally doped $YBa_2Cu_3O_{6+x}$. *Nature* **371**, 681 (1994).

24. Y. Ohta, T. Tohyama, S. Maekawa, Apex oxygen and critical temperature in copper oxide superconductors: Universal correlation with the stability of local singlets, *Physical Review B* **43**, 2968-2982 (1991).

25. E. Pavarini, I. Dasgupta, T. Saha-Dasgupta, O. Jepsen, O. Andersen, Band-Structure Trend in Hole-Doped Cuprates and Correlation with T_c max. *Physical Review Letters* **87**, 047003 (2001).

26. J. E. Hoffman *et al.*, A four unit cell periodic pattern of quasi-particle states surrounding vortex cores in $Bi_2Sr_2CaCu_2O_{8+\delta}$. *Science* **295**, 466 (2002).

27. C. V. Parker *et al.*, Fluctuating stripes at the onset of the pseudogap in the high-T_c superconductor $Bi_2Sr_2CaCu_2O_{8+x}$. *Nature* **468**, 677 (2010).

28. Y. Kohsaka *et al.*, How Cooper pairs vanish approaching the Mott insulator in $Bi_2Sr_2CaCu_2O_{8+\delta}$. *Nature* **454**, 1072 (2008).

29. J. E. Hoffman *et al.*, Imaging quasiparticle interference in $Bi_2Sr_2CaCu_2O_{8+\delta}$. *Science* **297**, 1148 (2002).

30. T. Hanaguri *et al.*, Quasiparticle interference and superconducting gap in $Ca_{2-x}Na_xCuO_2Cl_2$. *Nature Physics* **3**, 865 (2007).

31. E. Berg, D. Orgad, S. Kivelson, Route to high-temperature superconductivity in composite systems. *Physical Review B* **78**, 094509 (2008).

32. L. Goren, E. Altman, Enhancement of the critical temperature in cuprate superconductors by inhomogeneous doping. *Physical Review B* **84**, 094508 (2011).

33. T. Cren *et al.*, Influence of Disorder on the Local Density of States in High-T_c Superconducting Thin Films. *Physical Review Letters* **84**, 147 (2000).

34. C. Howald, P. Fournier, A. Kapitulnik, Inherent inhomogeneities in tunneling spectra of $Bi_2Sr_2CaCu_2O_{8+x}$ crystals in the superconducting state. *Physical Review B* **64**, 100504 (2001).

35. Q.-H. Wang, J. Han, D.-H. Lee, Pairing near the Mott insulating limit. *Physical Review B* **65**, 054501 (2001).

36. Z. Wang, J. Engelbrecht, S. Wang, H. Ding, S. Pan, Inhomogeneous d-wave superconducting state of a doped Mott insulator. *Physical Review B* **65**, 064509 (2002).

37. P. Richard *et al.*, Nature of oxygen dopant-induced states in high-temperature $Bi_2Sr_2CaCu_2O_{8+x}$ superconductors: A photoemission investigation. *Physical Review B* **74**, 094512 (2006).

38. C. Howald, H. Eisaki, N. Kaneko, A. Kapitulnik, Coexistence of periodic modulation of quasiparticle states and superconductivity in $Bi_2Sr_2CaCu_2O_{8+\delta}$. *Proceedings of the National Academy of Sciences of the U.S.A.* **100**, 9705 (2003).

39. A. Mesaros *et al.*, Topological Defects Coupling Smectic Modulations to Intra-Unit-Cell Nematicity in Cuprates. *Science* **333**, 426 (2011).

40. W. D. Wise *et al.*, Charge-density-wave origin of cuprate checkerboard visualized by scanning tunnelling microscopy. *Nature Physics* **4**, 696 (2008).

41. M. Boyer, Ph.D. Thesis, M.I.T. (2008).

42. J.-H. Ma *et al.*, Coexistence of Competing Orders with Two Energy Gaps in Real and Momentum Space in the High Temperature Superconductor $Bi_2Sr_{2-x}La_xCuO_{8+\delta}$. *Physical Review Letters* **101**, 207002 (2008).

43. M. J. Lawler *et al.*, Intra-unit-cell electronic nematicity of the high-T_c copper-oxide pseudogap states. *Nature* **466**, 347 (2010).

44. E. W. Hudson, S.-H. Pan, A. K. Gupta, K.-W. Ng, J. C. Davis, Atomic-scale quasi-particle scattering resonances in $Bi_2Sr_2CaCu_2O_{8+\delta}$. *Science* **285**, 88 (1999).

45. S.-H. Pan *et al.*, Imaging the effects of individual zinc impurity atoms on superconductivity in $Bi_2Sr_2CaCu_2O_{8+\delta}$. *Nature* **403**, 746 (2000).

46. E. W. Hudson *et al.*, Interplay of magnetism and high-T_c superconductivity at individual Ni impurity atoms in $Bi_2Sr_2CaCu_2O_{8+\delta}$. *Nature* **411**, 920 (2001).

47. E. W. Hudson *et al.*, STM study of novel resonances in $Bi_2Sr_2CaCu_2O_{8+\delta}$. *Physica B* **329-333**, 1365 (2003).

48. B. Koopman *et al.*, Scanning Tunneling Microscopy of Fe Doped $Bi_2Sr_2CaCu_2O_{8+x}$, *Bulletin of the American Physical Society* **57**, H37.6 (2012).

49. H. Eisaki *et al.*, Effect of chemical inhomogeneity in bismuth-based copper oxide superconductors, *Physical Review B* **69**, 064512 (2004).

50. J. W. Alldredge *et al.*, Evolution of the electronic excitation spectrum with strongly diminishing hole density in superconducting $Bi_2Sr_2CaCu_2O_{8+\delta}$, *Nature Physics* **4**, 319 (2008).

51. J. Alldredge, K. Fujita, H. Eisaki, S. Uchida, K. McElroy, Three-component electronic structure of the cuprates derived from spectroscopic-imaging scanning tunneling microscopy. *Physical Review B* **85**, 174501 (2012).

52. S.-H. Pan *et al.*, STM Studies of the Electronic Structure of Vortex Cores in $Bi_2Sr_2CaCu_2O_{8+\delta}$. *Physical Review Letters* **85**, 1536 (2000).

53. **Acknowledgements:** We thank Arun Bansil, Ivan Bozovic, Séamus Davis, Eric Hudson, Peter Hirschfeld, Aharon Kapitulnik, Dung-Hai Lee and Jouko Nieminen for useful discussions. J.E.H. acknowledges support from the NSF CAREER grant DMR-0847433 and AFOSR PECASE grant FA9550-06-1-0531. G.D.G. acknowledges support from the US Department of Energy under contract DE-AC02-98CH10886. R.S.M. acknowledges support from the US Department of Energy under contract DE-FG02-07ER46352.

Figure captions

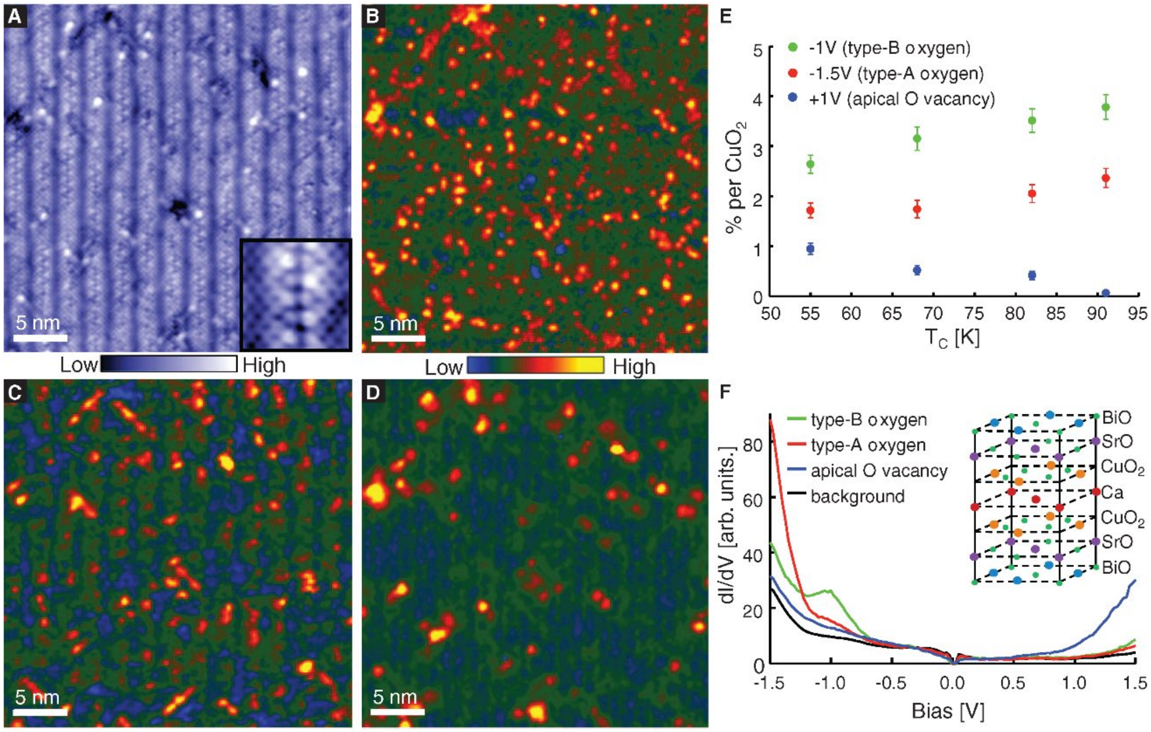

Fig. 1. (A) Atomically resolved topographic image of BSCCO with T_c=55K, acquired at V_{sample}=+1V and I_{set}=150pA over a 35nm area (inset: 3x magnification). **(B-D)** dI/dV images in the same area as (A), acquired at V_{sample}=-1V, -1.5V, and +1V respectively. **(E)** Density of each type of dopant imaged within the 4 samples studied. **(F)** dI/dV spectra over each dopant type, from T_c=82K sample. Each colored spectrum is the average of all imaged dopants of its type within a 30 nm field of view (FOV); the black trace shows the average spectrum far from dopants. Inset shows the top half of the BSCCO unit cell.

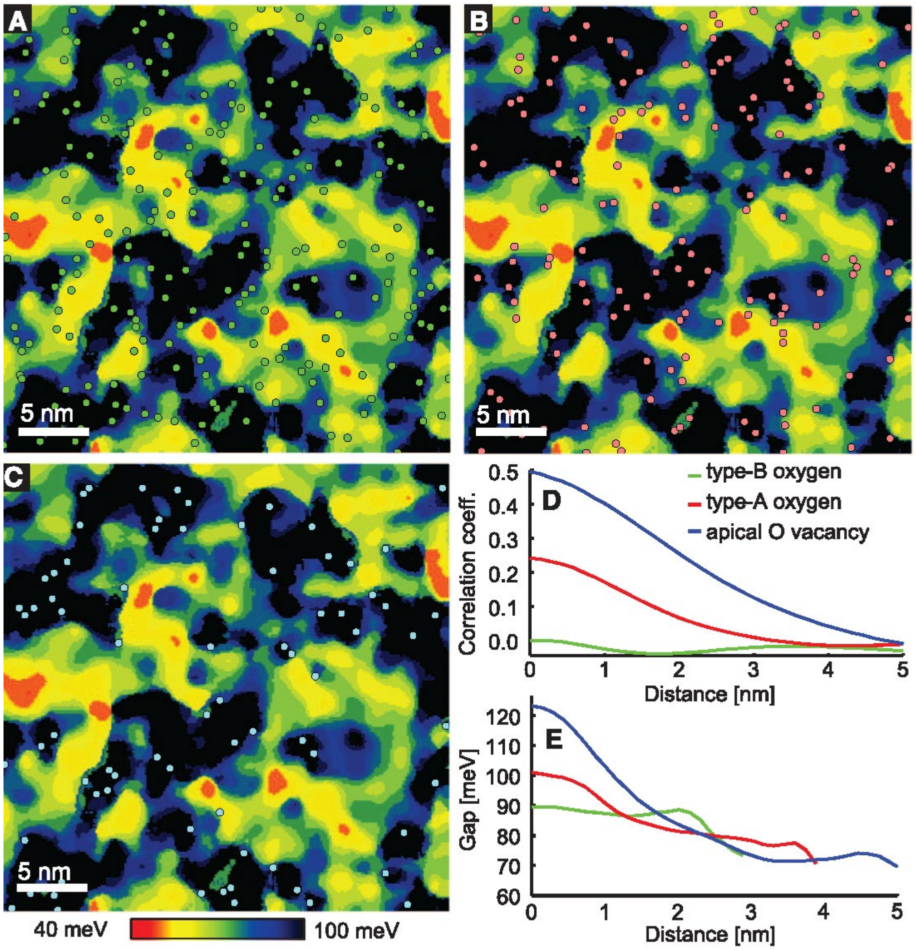

Fig. 2. Comparison of dopant locations and PG map. Locations of **(A)** type-B interstitial oxygens (green circles), **(B)** type-A interstitial oxygens (red circles), and **(C)** apical oxygen vacancies (blue circles) superimposed on top of the PG map of the T_c=55K sample. **(D)** Cross-correlation coefficient relating the PG to the distance to the nearest dopant. **(E)** Average PG vs. distance from the nearest dopant of each type. In (D-E), green, red, and blue lines represent type-B oxygens, type-A oxygens, and apical oxygen vacancies, respectively.

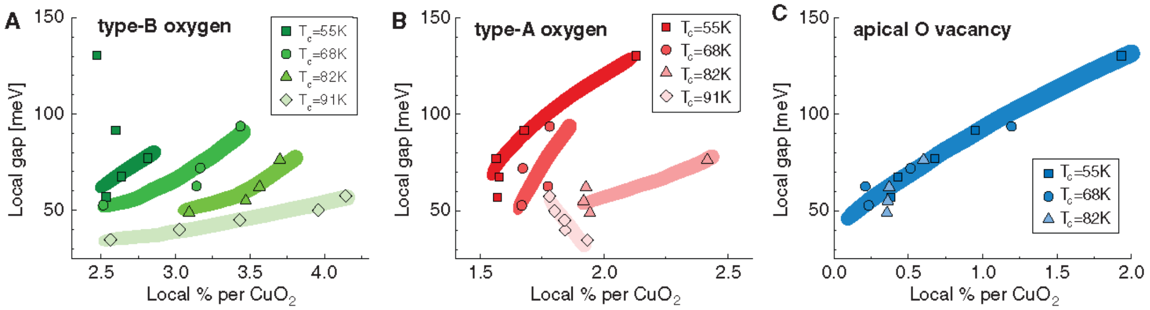

Fig. 3. Local PG vs. local dopant density. For each sample, we create a local density map of the number a given dopant type per region of radius ξ ~ 2nm. The values in the density map are then binned based on the PG value at the corresponding pixel. The average PG value in each bin is then plotted vs. the average dopant density value within each bin. **(A)** Local PG vs. local density of type-B interstitial oxygen dopants, from the 4 different samples used in this study. **(B)** Local PG vs. local density of type-A interstitial oxygen dopants, from the 4 different samples used in this study. **(C)** Local PG vs. local density of apical oxygen vacancies, from the 3 underdoped samples used in this study. Trend lines in (A-C) are guides to the eye.

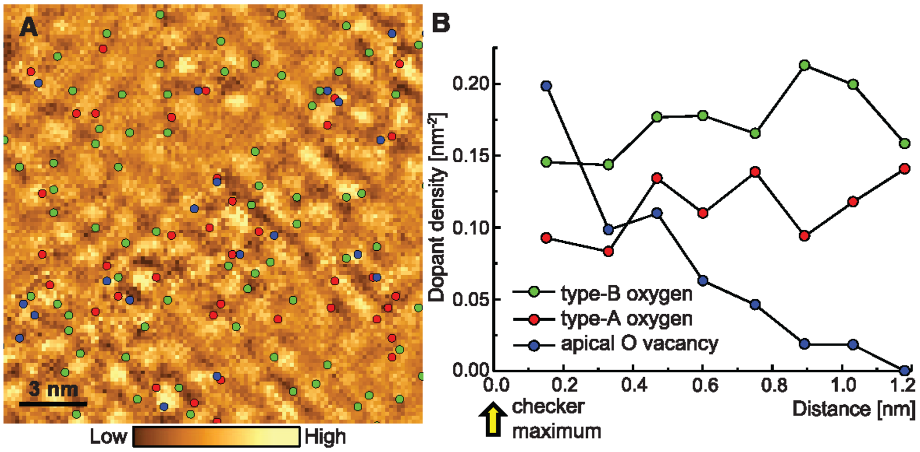

Fig. 4. Comparison of dopant locations and the checkerboard. **(A)** Fourier-filtered dI/dV image of the T_c=55 K sample at +36 mV, showing a clear CB (setup: V_{sample}=-150 mV; I=800 pA). Type-B oxygens, type-A oxygens, and apical oxygen vacancies are superimposed as green, red, and blue circles respectively. **(B)** Dopant density of each type vs. distance from the center of the nearest CB maximum.

Supplementary Materials
Zeljkovic *et al*, Science 337, 320 (2012)

(I) Global vs. local doping trends

Prompted by the discovery of nanoscale inhomogeneity in BSCCO (*4,5,33,34*), several theoretical models (*3,35,36*) qualitatively reproduced the observed inhomogeneity by assuming that interstitial oxygen dopants contribute localized holes, which locally reduce the dominant spectroscopic gap, in accordance with the global trend established by measurements which average over many coherence lengths (*12,13*).

Startlingly, McElroy's breakthrough work in 2005 (*8*) which first imaged the interstitial oxygen dopants themselves (*37*), showed the opposite local trend: the imaged oxygens were correlated with regions of large gap. This new experimental fact was explained by a new model in which the interstitial oxygen's dominant local effect is strain, which increases the local superexchange $J(\vec{r})$, which increases the local pairing strength (*18*). A follow-up clarified that within this model, the oxygen dopants do accumulate local holes, which serve primarily to reduce the height of the coherence peaks via enhancement of the fermionic bandwidth and formation of an impurity bound state at the edge of the spinon band. But it was found that without including a phenomenological increase of pairing strength near the dopants, with specific length scale $0.5a_0$, the experimental data could be reproduced (*19*). In summary, this carefully tuned model which reconciles the counter-intuitive experimental correlation between dopant locations and regions of large gap, paints a picture in which local holes are correlated with large gap. It is important to note that McElroy's experiment measures the locations of the dopants themselves, but does not directly measure the local hole concentration.

An independent measure of the local hole concentration can be obtained from local studies of the disordered static electronic modulation. This modulation has been termed 'checkerboard' (*26*), 'fluctuating stripes' (*27,38*), 'electronic glass' (*28*), 'smectic' (*39*), or 'charge density wave' (*40*); for simplicity we have used the phenomenological term 'checkerboard' (CB). In both double (*28*) and single (*40*) layer BSCCO, doping dependent studies show that the global average CB wavevector tracks the antinodal nesting wavevector, which is a measure of the size of the hole pocket and thus the global hole concentration. However, the CB is quite disordered, with local wavevector (defined as $2\pi/\lambda_c$ where λ_c is the real space distance between adjacent crests of the modulation) varying by ~10%, even from one period to the next. Wise *et al* discovered that the local pseudogap (PG) correlates strongly with the local CB wavevector, following the global trend. This demonstrates that the local checkerboard wavevector is a meaningful quantity, not just randomly varying due to pinning by disorder. This suggests that the local CB wavevector is a good measure of the local antinodal nesting and the size of the hole pocket, and thus the first direct measure of the local hole concentration (*7*).

Combining the conclusions of the McElroy and Wise experiments, the direct measure of the local hole concentration shows that local holes are correlated with regions of small PG (*7*), and the direct measure of the interstitial oxygen locations shows that the -1V interstitial oxygens are correlated with regions of large gap (*8*). Therefore, the -1V interstitial oxygens anti-correlate with local holes!

We supported this counter-intuitive conclusion in Fig. 3. For each of our four samples with T_c=55K, 68K, 82K, and 91K, we created a density map of type-B oxygens as follows. Each pixel in the density map was assigned a value by counting the number of dopants within a circle of radius ξ ~ 2nm, centered at that pixel, and dividing by the number of CuO_2 plaquettes in the circle. The values (pixels) in the density map were then sorted into 4-5 bins based on the PG value at the corresponding pixel in the simultaneous PG map. The average gap value in each bin was then plotted vs. the average density value within each bin, to produce Fig. 3.

Fig. 3 demonstrates that in underdoped samples, the local hole concentration, which in turn determines the checkerboard wavevector and the PG energy, is set primarily by the local removal of holes by the apical oxygen vacancies, rather than the donation of holes from the interstitial oxygens. The interstitial oxygens do contribute delocalized holes, but the interstitial oxygen positions remain correlated to regions of decreased local hole concentration due to their tendency to remain close to the apical oxygen vacancies, as in Frenkel defects.

We conclude this section by commenting on the relationship between local PG and superconductivity. Although numerous measurements (*12,13*), including T-dependent STM (*41*), show a global anti-correlation between PG and SC energy scales, STM work to date has been inconclusive on the local relationship between PG and SC gap. One STM experiment claims that the SC gap remains homogeneous despite PG inhomogeneity (*10*); another claims local correlation between PG and SC gap (*42*). However, we caution that under typical experimental conditions the exact energy of the SC gap is very challenging to extract from the strong PG background in STM spectra, and additional work should be done to clarify this relationship.

(II) Identity of +1V atomic features

Chemical disorder in $Bi_{2+y}Sr_{2-y}CaCu_2O_{8+x}$ (BSCCO) falls into two categories: cation disorder and oxygen disorder. Mitzi *et al* grew single crystal BSCCO with several cation substitutions (e.g. La for Sr, Y for Ca, excess Bi for Sr), and also explored several annealing recipes for changing the oxygen concentration (*21*). The cation concentration was checked using wavelength dispersive microprobe analysis [electron-probe-microanalysis technique (EMPA), using a JEOL superprobe 773] which gave the concentration of each cation with ±4% accuracy. Microprobe analysis was employed on several crystals before and after annealing at temperatures up to 840°C, but no change in cation concentration was ever detected. Since our samples were annealed only at the comparably modest temperature of 550°C, it is unlikely that the cation concentration varies between our 4 samples.

We observe systematic variation in the concentration of +1V features with annealing, which suggests that these features represent oxygen disorder. Oxygen disorder falls into two categories: interstitials and site vacancies. Interstitials should be negatively charged, therefore should have resonance states below the Fermi level. Furthermore, they should decrease in concentration when the sample is annealed in vacuum. On the other hand, oxygen site vacancies should be positively charged relative to the filled site, and should increase in concentration when the sample is annealed in vacuum. The observed features in question have spectroscopic signatures starting around +0.8eV above the Fermi level, and they increase in concentration when the sample is annealed in vacuum. We therefore conclude that these +1V features are oxygen lattice site vacancies.

We consider the 3 distinct oxygen lattice sites. To determine the exact lateral positions of the atomic-scale features appearing in differential conductance maps at energies higher than +0.8eV, we first utilize Lawler's algorithm (*43*) on each dataset to locate each Bi atom with picoscale accuracy. When Lawler's algorithm is used with correction length scale Λ greater than the supermodulation wavelength $\lambda_{SM}{\sim}7a_0$, the effect is to remove the inevitable slow thermal and piezo drift which occur during a multi-hour map, without altering the true structure of the surface. However, for the purpose of locating the dopant features within the unit cell, we need a 'perfect' square grid. We therefore choose a short correction length scale Λ ~ a_0 which removes both the slow drift which is an experimental artifact, and also most of the real lateral distortion of the supermodulation, as seen in Fig. S1.

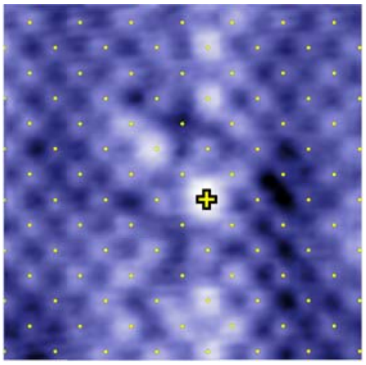

Fig. S1. Drift-corrected BSCCO topography (V_{sample} = 600pA, I_{set} = +150mV) over a 4nm area, with a perfect square lattice of small yellow circles superimposed. The yellow cross denotes the position of one +1V feature. The brightness of this spot suggests that the +1V feature is not a missing Bi atom.

We next perform a Gaussian fit to find the center of each feature in the +1V dI/dV map, and determine its lateral location with respect to the nearest atoms in the corrected topography. We directly compare the +1V feature locations to each of the 3 distinct O lattice sites, illustrated in Fig. S2A. Fig. S2B-F shows the lateral position of each +1V feature within the unit cell, for two samples. Due to the large size of the dopant (full width at half max ~ 0.75 nm, compared to the 0.383 nm unit cell size), and due to the difficulty in removing 100% of the supermodulation distortion, there remains some scatter in the lateral locations, but we are still able to distinguish clearly between the 3 possible O sites. We find that the +1V features are consistent only with the apical oxygen site. This conclusion is reinforced by plotting the density of observed +1V features vs. distance from each of the 3 possible O sites, in Fig. S3.

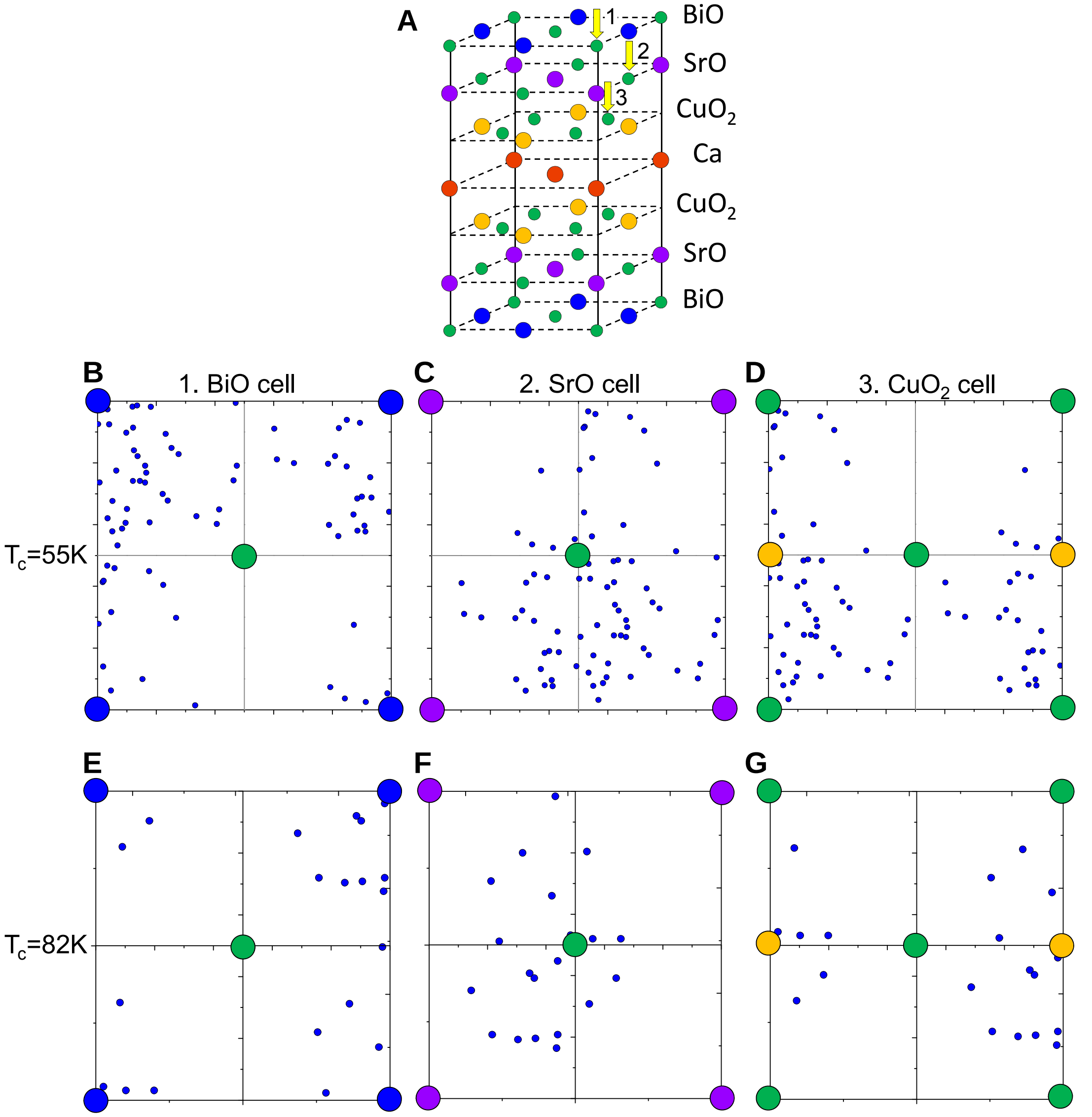

Fig. S2. (A) Top half of BSCCO unit cell, showing the 3 inequivalent oxygen sites. Positions of each localized +1V feature (blue dots) within a single unit cell in one sample with T_c=55K **(B-D)** and another sample with T_c=82K **(E-G)**. For each sample, the same set of +1V features is replotted 3 times, with respect to each layer, to emphasize its relation to the 3 inequivalent oxygen lattice sites. **(B,E)** are plotted with respect to the BiO layer (Bi: blue; O:green); **(C,F)** are plotted with respect to the SrO layer (Sr: purple; O: green); **(D,G)** are plotted with respect to the CuO_2 layer (Cu: orange; O: green). Both samples show that the +1V features are centered around the apical O, in the SrO layer. (Note: it is clear that the +1V features are not located at the purple Sr site, and therefore can't be Bi^{3+} substitutions at the Sr^{2+} site.)

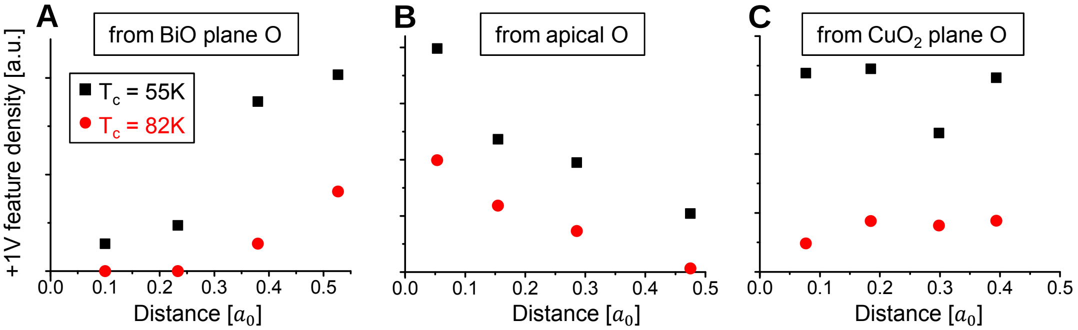

Fig. S3. Areal density of +1V features as a function of lateral distance from each of the 3 distinct oxygen lattice sites, for two samples with T_c=55K (black squares) and T_c=82K (red circles). Areal density is shown as a function of distance from the **(A)** O site in the BiO layer; **(B)** apical O site in the SrO layer; and **(C)** O site in the CuO_2 layer. The areal density is clearly peaked at the apical O site in (B).

Finally, we revisit the possibility of cation disorder, which is not completely eliminated within the accuracy of the microprobe analysis (*21*). The lateral location of the +1V features is clearly peaked at the Bi or Cu sites (Fig. S3B) and not at the Sr or Ca sites (Fig. S3A). It is well known that defects at the Cu site produce strong low-bias resonances (*44-48*), which are not observed in our data (Fig. S4E, inset). Regarding defects at the Bi site: Bi vacancies are unlikely due to the fact that the sites in question appear bright rather than dark in topographic images (Fig. S1). Substitutions at the Bi site are unlikely because Bi concentration actually exceeds the stoichiometric factor per unit cell (starting growth ratio of Bi:Sr is 2.1:1.9). It seems further unlikely that defects at this type-B cation site, so far from the CuO_2 plane, would have such a tremendous effect on the PG when type-B interstitial oxygens have already been demonstrated by our work to have minimal effect on PG, and type-B cation substitutions have been demonstrated by transport experiments to have little effect on T_c (*49*).

In summary, the lateral position of +1V features shown in Figs. S2 and S3 rules out defects at the Sr and Ca sites, and at the oxygen sites in the BiO and CuO_2 layers. Low energy spectroscopy rules out defects at the Cu sites. Topographic information suggests that defects at the Bi site are an unlikely explanation. The only remaining site is the apical O site. Our count of concentration vs. T_c, combined with prior findings from wavelength dispersive microprobe analysis on annealed samples (*21*), strongly supports the identification of the +1V features as apical O site vacancies. We suggest that scanning transmission electron microscopy with electron energy loss spectroscopy could be used on a single-unit-cell thick BSCCO sample to further support this identification.

(III) High-bias spectra at different setup conditions

To prove the reproducibility of each of the "typical" dopant spectra shown in Fig. 1F, we acquire full spectra at both positive and negative bias setup condition for five different dopants of each type. The spectral shape is consistent between the two setup conditions, and does not vary considerably among the same group of dopants, as shown in Fig. S4.

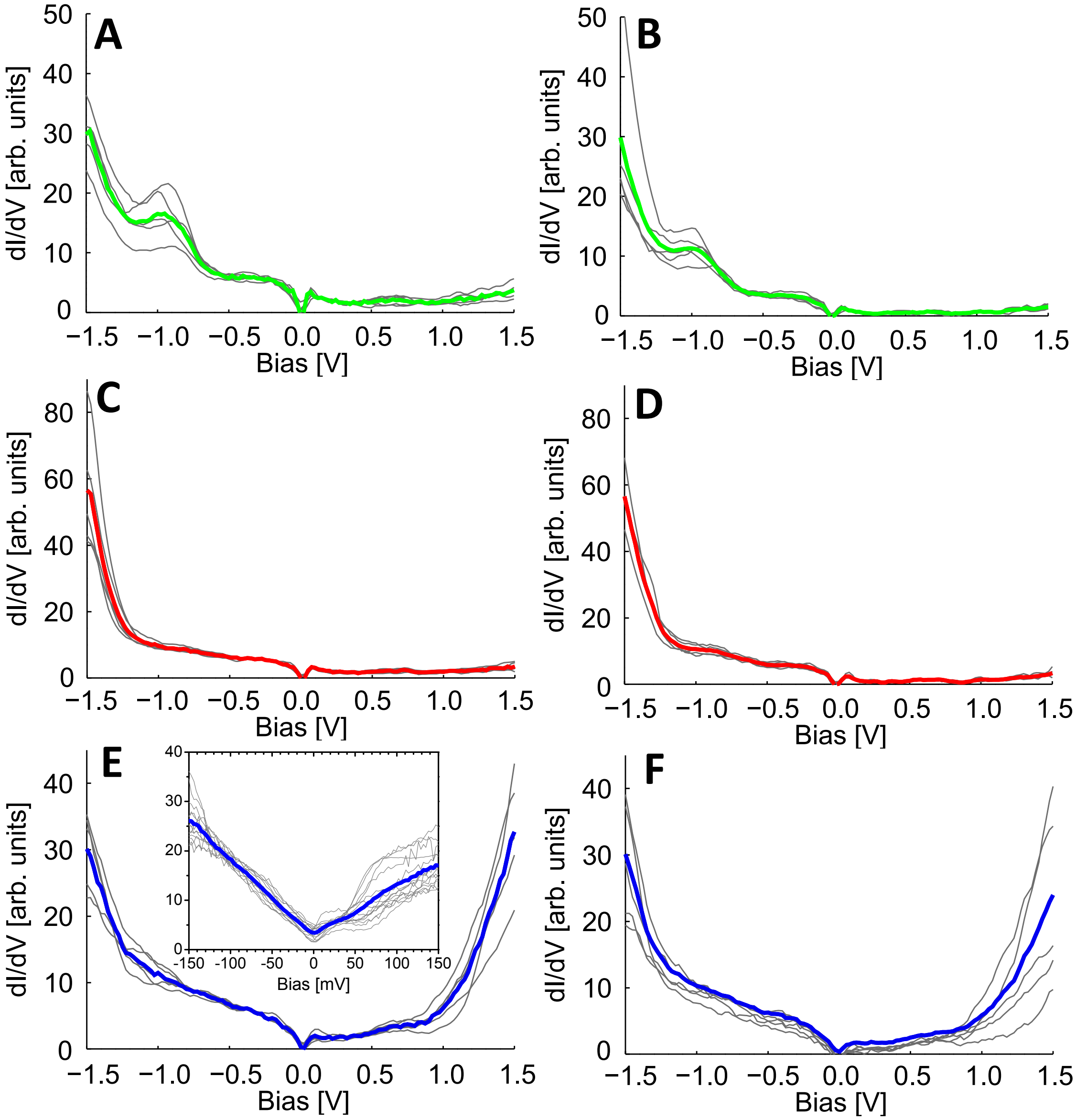

Fig. S4. High-bias spectra plotted for each of the three dopant types at two different setup conditions, for T_c=82K sample. Dark gray curves in all panels represent spectra from five different locations of the same dopant type, and the bold, colored curve is their average. The left column shows spectra taken with setup condition V_{sample} = -650mV, I=260 pA, whereas the right column shows spectra acquired with setup condition V_{sample} = +650mV, I=60 pA. **(A)** and **(B)** show spectra on top of type-B interstitial oxygens; **(C)** and **(D)** show spectra on top of type-A interstitial oxygens; **(E)** and **(F)** show spectra on top of apical oxygen vacancies. Inset to **(E)** zooms in on the low energy conductance of several +1V features at T_c=55K, demonstrating the absence of near-ε_F resonances at the +1V features (setup: V_{sample}=-150 mV; I=800 pA).

(IV) PG determination

A number of different fitting techniques have been employed to extract the PG energy Δ_1 from raw STM spectra in previous studies (*11,51,52*). However, without an accepted microscopic model for the PG, it is hard to justify the computationally intensive effort required for the use of any specific fitting function. We therefore use a simple, two part algorithm to extract the apparent PG energy Δ_1 from the positive bias conductance (empty states) between ε_F and +150 meV. For such spectra in which the global maximum in conductance lies between ε_F and +80 meV, this typically corresponds to a clear gap-edge peak, so we set Δ_1 equal to this energy. For spectra in which the global maximum in conductance occurs at energy greater than 80 meV, there is typically no clear gap-edge peak, so we instead set Δ_1 equal to the energy of the kink where the conductance slope abruptly flattens.

To demonstrate the reliability of this simple PG extraction algorithm, we focus on the most challenging sample, with T_c=55K, where we identify clear gap-edge peaks at $\Delta_1 \leq 80$ meV in only 55% of the spectra. From this sample, we show examples of typical spectra and their extracted Δ_1 in Fig. S5. As a further demonstration, we bin all spectra by Δ_1, with bin size determined by the energy spacing at which the data was acquired. Fig. S6 shows the complete set of spectra in each of 4 bins, exemplifying the quantitative spread but qualitative similarity of most spectra within each bin.

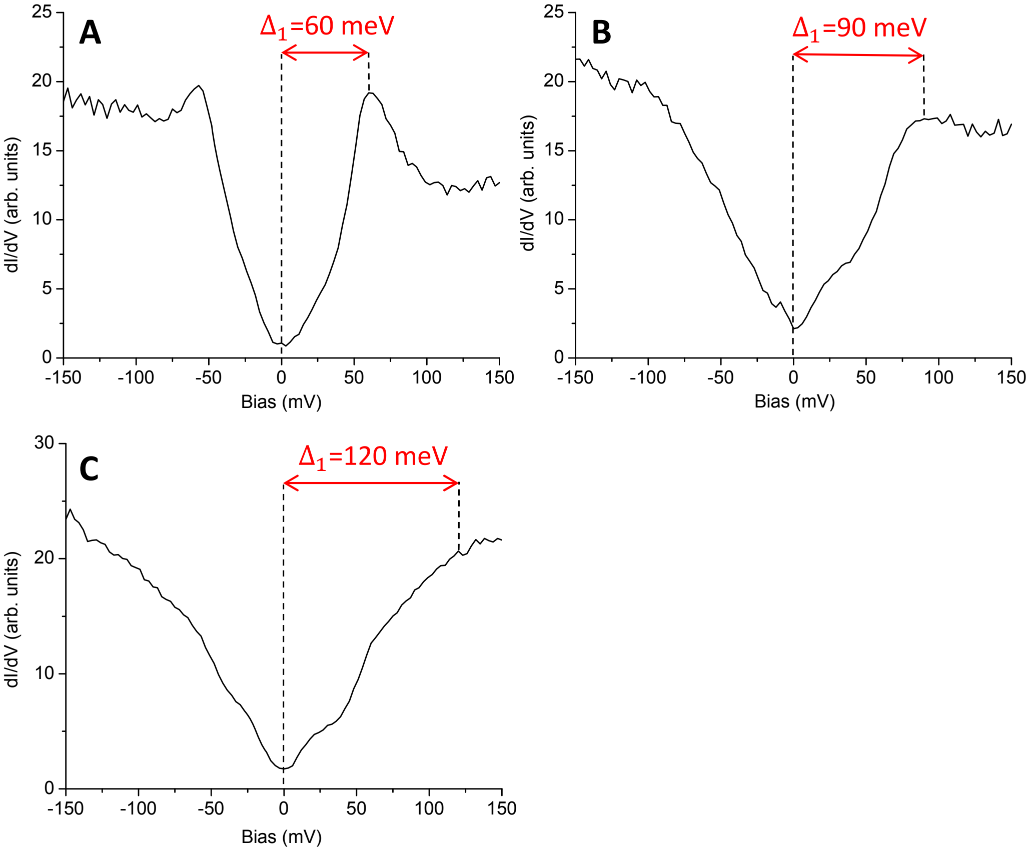

Fig. S5. Typical spectra from T_c=55 K sample, exemplifying the extraction of Δ_1. (Setup V_{sample}=-150 meV and I_{set} = 800 pA.) All spectra have been 3 pixel boxcar averaged (9 spectra are averaged together, effectively smoothing on a 0.48 nm length scale). **(A)** Δ_1=60 meV is obtained as the location of the global maximum on the positive side of the spectrum. **(B-C)** Δ_1=90 and Δ_1=120 meV are each obtained as the position of the first local maximum beyond 80 meV, which is typically an effective marker of the kink where the conductance slope flattens.

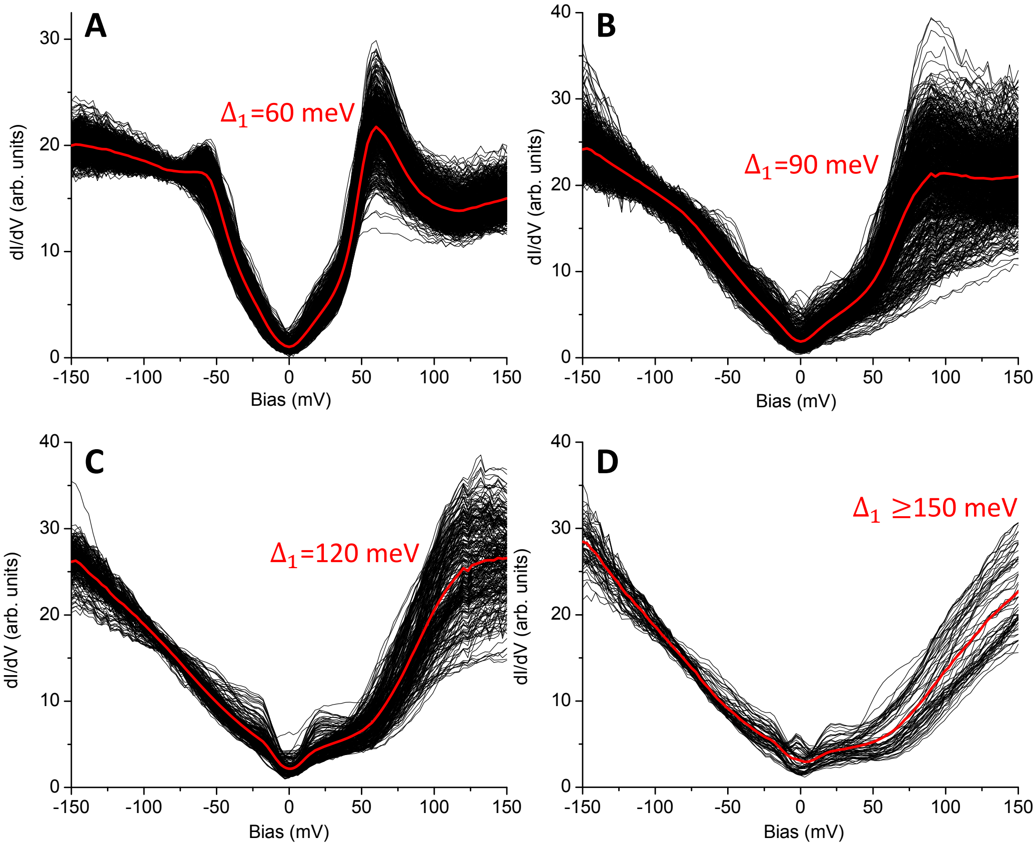

Fig. S6. Binned spectra from T_c=55K sample, demonstrating the quantitative variation but qualitative similarity of each group of spectra assigned a common Δ_1. (Setup V_{sample}=-150 meV and I_{set} = 800 pA.) All black spectra have been 3 pixel boxcar averaged (9 spectra are averaged together, effectively smoothing on a 0.48 nm length scale). The bold, red curve in each panel represents the average of all the individual black spectra shown in that panel. **(A)** Δ_1=60 meV bin; **(B)** Δ_1=90 meV bin; **(C)** Δ_1=120 meV bin; **(D)** Δ_1 ≥150 meV bin.

Because the slope-compare algorithm used for Δ_1> 80 meV is more sensitive to the noise level than the global maximum algorithm for $\Delta_1 \leq 80$ meV, we estimate the error of our Δ_1 extraction by repeating the same algorithm on increasingly smoothed data, and comparing results. Our final Δ_1 maps (shown in Fig. S7 and used in Figs. 2 and 3) are determined from spectral surveys that have been smoothed with a 3 pixel boxcar average (corresponding to 0.48-0.69 nm, depending on the dataset, which is still far less than the superconducting coherence length ξ~2.2 nm (*52*)). The pixel-by-pixel RMS differences between these Δ_1 maps and analogous Δ_1 maps from spectra surveys smoothed with 5 pixel boxcar average (~1 nm) are 12.1, 9.6, 4.9, and 2.7 meV from the T_c = 55, 68, 82, and 91K samples, respectively. In summary, we estimate that the PG extraction error is largest (up to ~12 meV) in the T_c=55K sample, and decreases to < 3 meV in the T_c=91K sample.

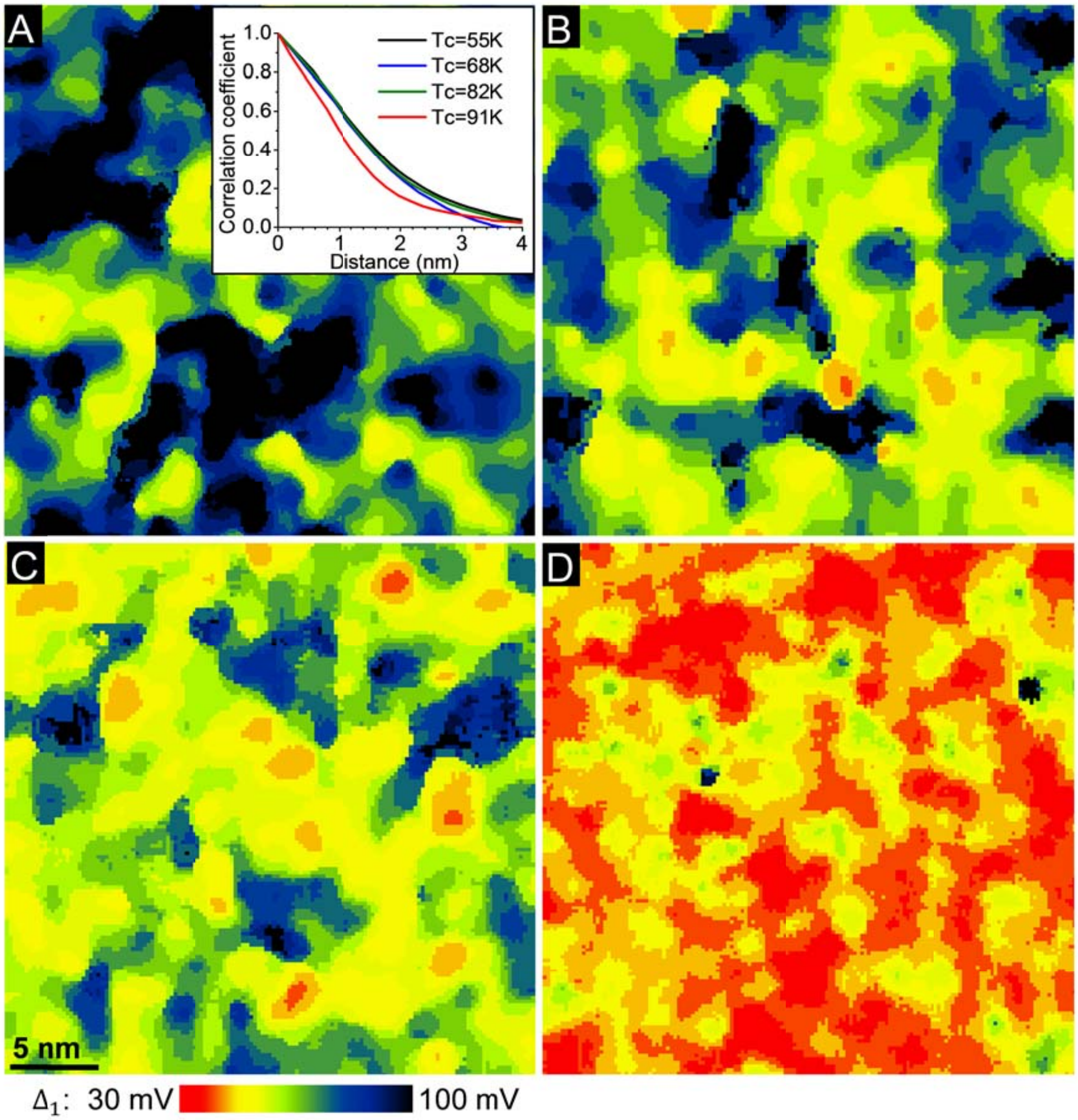

Fig. S7. Extracted Δ_1 map for **(A)** T_c=55K; **(B)** T_c=68K**;** **(C)** T_c=82K; **(D)** T_c=91K. All maps are 30 nm x 30 nm, and all are displayed using the same colorscale. Inset to **(A)** shows the autocorrelation of each gapmap, demonstrating a length scale ~2-3 nm. This justifies our initial smoothing of the spectral survey on the ~0.5-0.7 nm length scale, to reduce noise in each spectrum and ensure the reliability of the Δ_1 extraction algorithm.

(V) Relation of dopants to PG

To correlate the PG map $\Delta_1(\vec{r})$ with the locations of the dopants, one possibility would be to correlate directly with the dI/dV map at the relevant energy. However, some dopants of the same type appear with slightly different size or brightness (see scatter in Fig. S4) which might weight the cross-correlation unintentionally in favor of a subset of dopants. Instead, we create two-dimensional maps $D_A(\vec{r})$, $D_B(\vec{r})$, and $D_v(\vec{r})$ of the distance from the nearest type-A oxygen, type-B oxygen, and apical oxygen vacancy, respectively. We compute the cross-correlation $C(\vec{R})$ between the PG map $\Delta_1(\vec{r})$ and each distance map $D(\vec{r})$ using the standard formula:

$$C(\vec{R}) = -\frac{\int [D(\vec{r}) - \overline{D}] \times \left[\Delta_1(\vec{r} + \vec{R}) - \overline{\Delta_1}\right] d^2r}{\sqrt{A_{D,D}(0) A_{\Delta,\Delta}(0)}}$$

$$A_{D,D}(\vec{R}) = \int [D(\vec{r}) - \overline{D}] \times \left[D(\vec{r} + \vec{R}) - \overline{D}\right] d^2r$$

Fig. S8 shows large positive correlation between apical oxygen vacancies and the PG for the three underdoped samples. Type-A oxygen dopants are correlated to a lesser extent, while type-B oxygen dopants exhibit very weak correlation with the PG. From the correlation length scales shown in Fig. 2D and Fig. S8, we see that the apical oxygen vacancies influence the PG on a ~2-3 nm length scale, and we speculate that they will also impact the superconducting state on this length scale. This is consistent with the PG map correlation length $\xi_{PG} \sim$2-3 nm (Fig. S7A inset), and with measurements of the superconducting coherence length $\xi_{SC} = 2.2 \pm 0.3$ nm (*52*).

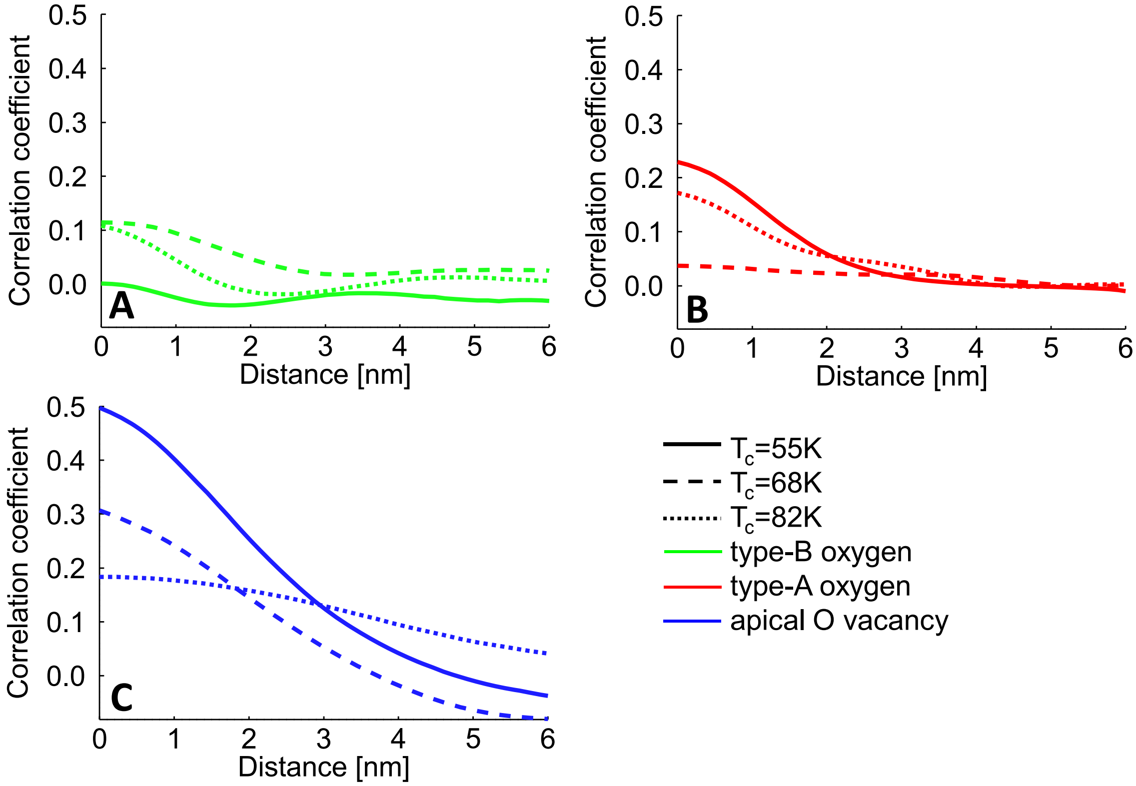

Fig. S8. Cross-correlation of the PG map $\Delta_1(\vec{r})$ and the map of distance to the nearest dopant of **(A)** type-B oxygen; **(B)** type-A oxygen; and **(C)** apical oxygen vacancy. Different curves within each panel represent data taken on different underdoped samples (solid: 55K; dashed: 68K; and dotted: 82K).

As a check, we employ a second method to view the same information as in Fig. S8. From a given distance map $D(\vec{r})$, we bin the pixels based on their distance, then apply this binning to the corresponding PG map $\Delta_1(\vec{r})$, and compute the average gap within each distance bin. Fig. S9 shows the average gap as a function of distance from the nearest impurity of each type.

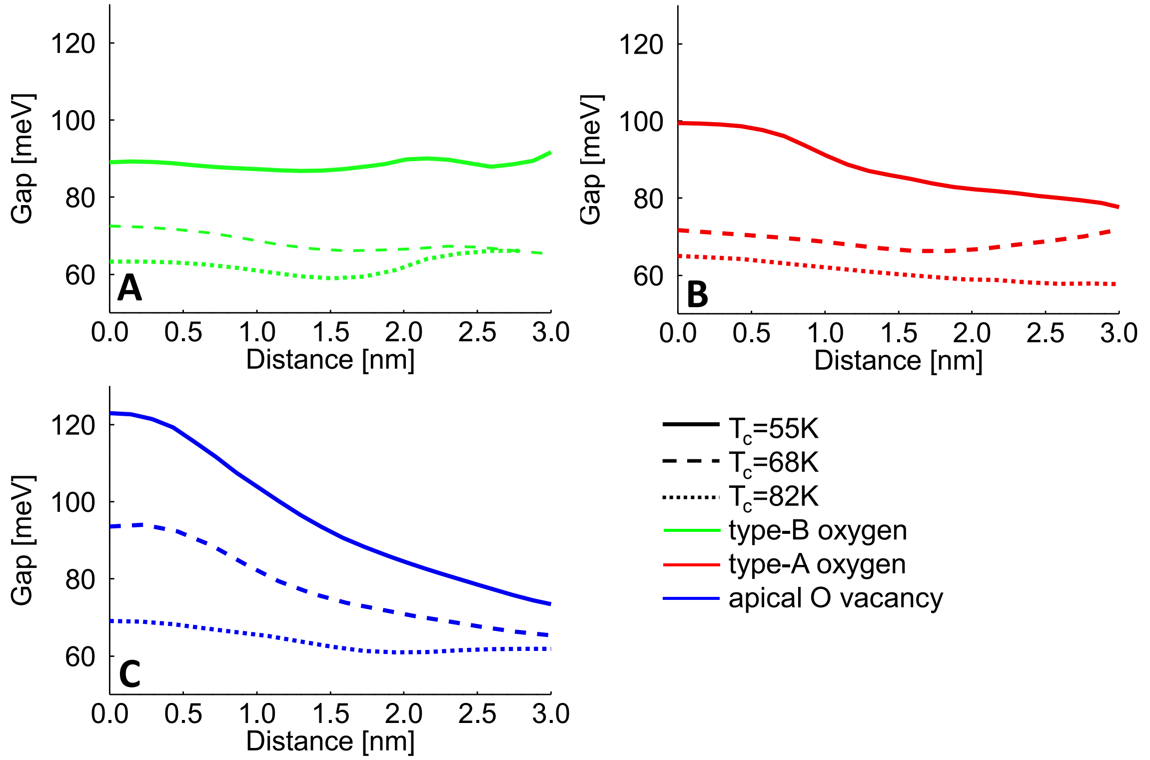

Fig. S9. Average PG as a function of distance from **(A)** type-B oxygens; **(B)** type-A oxygens; and **(C)** apical oxygen vacancies, respectively. Different curves within each panel represent data taken on different underdoped samples (solid: 55K; dashed: 68K; and dotted: 82K).

(VI) Relation of dopants to checkerboard

In order to determine whether the dopants play a role in pinning the checkerboard, we first disentangle the long-range DOS variation (length scale > $10a_0$) in the dI/dV maps from the checkerboard itself (typical wavelength $\lambda_c \sim 4a_0$), as demonstrated in Fig. S10.

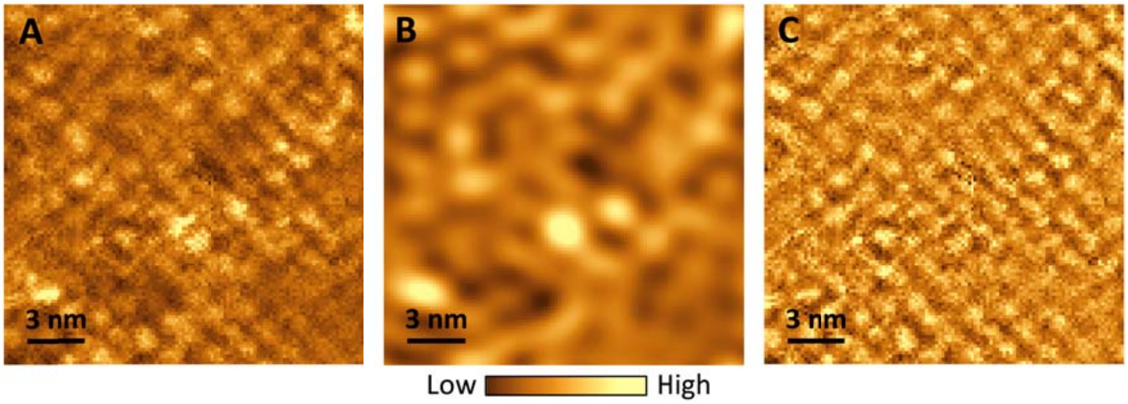

Fig. S10. Raw and filtered differential conductance. **(A)** Raw dI/dV image from T_c=55K, at energy +36mV, with setup V_{sample} = -150 mV and I_{set} = 800 pA. **(B)** Fourier-filtered image that contains only the wavevectors smaller than $2\pi/(10a_0)$. **(C)** Quotient of image (A) divided by image (B).

From the Fourier-filtered differential conductance image, it is easy to determine the centers of the 'checkers' (Fig. S11A), and calculate the distance from each impurity to the center of the nearest 'checker' (Fig. S11B). To produce Fig. 4B, we histogrammed the number of occurrences of each dopant type with respect to the distance *d* from the nearest 'checker', and normalized the count by the probability that any pixel would lie a distance *d* from a 'checker'.

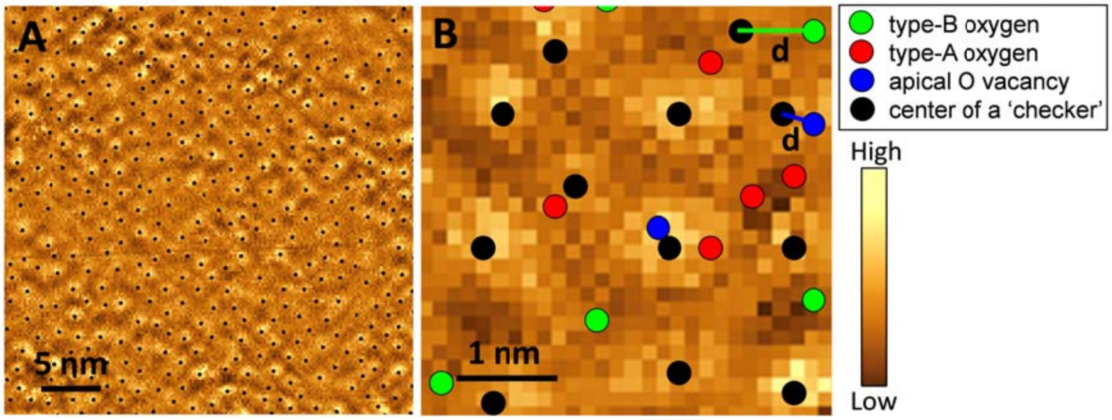

Fig. S11. Dopant proximity to the peaks of the checkerboard. **(A)** Fourier-filtered dI/dV image from T_c=55K sample, at energy +35 mV, with setup V_{sample} = -150 mV and I_{set} = 750 pA. The center of each peak is shown with a superimposed black circle. **(B)** Zoom on 4nm sub-FOV of the image in (A), exemplifying the distance of the dopants to the nearest checkerboard peak.

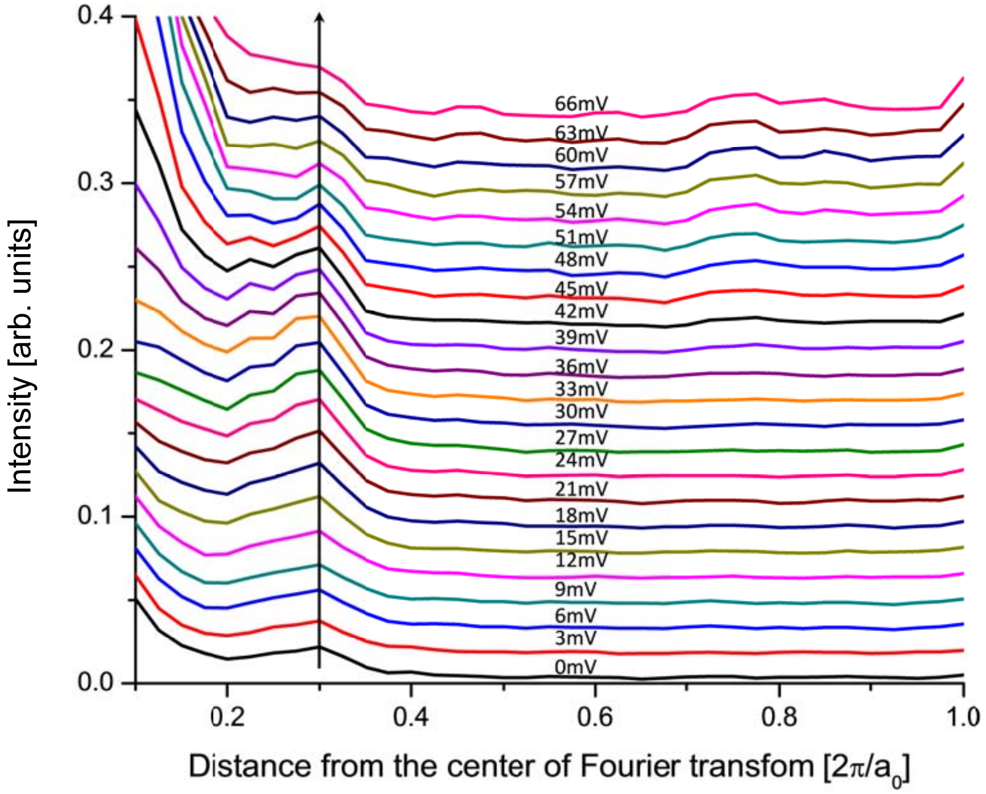

Fig. S12. Energy dependent linecut through the Fourier transform of the tunneling conductance $g(\vec{q},V)$, along the Cu-O-Cu direction from $\vec{q}=0$ to the Bragg peak, demonstrating the non-dispersing, incommensurate CB feature around $\vec{q}\sim 0.3$. Data was acquired on the T_c=55K sample, with setup V_{sample}=800pA and I=-150mV.

Because the CB does not disperse with energy, as shown in Fig. S12, the analysis and conclusions about CB pinning are insensitive to the exact energy used for imaging the CB. (Because our samples are very clean, having no Cu site substitutions producing near-ε_F resonances within a typical 30 nm FOV, we see no dispersing QPI at energies within the superconducting gap.) We also have verified that the dopant-CB pinning relationships hold for the T_c=82K sample.

References

1. E. Dagotto, Complexity in strongly correlated electronic systems. *Science* **309**, 257 (2005). doi:10.1126/science.1107559 Medline

2. V. J. Emery, S. A. Kivelson, O. Zachar, Spin-gap proximity effect mechanism of high-temperature superconductivity. *Phys. Rev. B* **56**, 6120 (1997). doi:10.1103/PhysRevB.56.6120

3. I. Martin, A. Balatsky, Doping-induced inhomogeneity in high-T_c superconductors. *Physica C* **357-360**, 46 (2001). doi:10.1016/S0921-4534(01)00192-7

4. S.-H. Pan *et al.*, Microscopic electronic inhomogeneity in the high-T_c superconductor $Bi_2Sr_2CaCu_2O_{8+x}$. *Nature* **413**, 282 (2001). doi:10.1038/35095012 Medline

5. K. M. Lang *et al.*, Imaging the granular structure of high-T_c superconductivity in underdoped $Bi_2Sr_2CaCu_2O_{8+\delta}$. *Nature* **415**, 412 (2002). doi:10.1038/415412a Medline

6. K. K. Gomes *et al.*, Visualizing pair formation on the atomic scale in the high-T_c superconductor $Bi_2Sr_2CaCu_2O_{8+\delta}$. *Nature* **447**, 569 (2007). doi:10.1038/nature05881 Medline

7. W. D. Wise *et al.*, Imaging nanoscale Fermi-surface variations in an inhomogeneous superconductor. *Nat. Phys.* **5**, 213 (2009). doi:10.1038/nphys1197

8. K. McElroy *et al.*, Atomic-scale sources and mechanism of nanoscale electronic disorder in $Bi_2Sr_2CaCu_2O_{8+\delta}$. *Science* **309**, 1048 (2005). doi:10.1126/science.1113095 Medline

9. K. McElroy *et al.*, Coincidence of checkerboard charge order and antinodal state decoherence in strongly underdoped superconducting $Bi_2Sr_2CaCu_2O_{8+\delta}$. *Phys. Rev. Lett.* **94**, 197005 (2005). doi:10.1103/PhysRevLett.94.197005 Medline

10. M. C. Boyer *et al.*, Imaging the two gaps of the high-temperature superconductor $Bi_2Sr_2CuO_{6+x}$. *Nat. Phys.* **3**, 802 (2007). doi:10.1038/nphys725

11. A. Pushp *et al.*, Extending universal nodal excitations optimizes superconductivity in $Bi_2Sr_2CaCu_2O_{8+\delta}$. *Science* **324**, 1689 (2009). doi:10.1126/science.1174338 Medline

12. G. Deutscher, Coherence and single-particle excitations in the high-temperature superconductors. *Nature* **397**, 410 (1999). doi:10.1038/17075

13. S. Hüfner, M. A. Hossain, A. Damascelli, G. A. Sawatzky, Two gaps make a high-temperature superconductor? *Rep. Prog. Phys.* **71**, 062501 (2008). doi:10.1088/0034-4885/71/6/062501

14. T. Kondo, R. Khasanov, T. Takeuchi, J. Schmalian, A. Kaminski, Competition between the pseudogap and superconductivity in the high-T_c copper oxides. *Nature* **457**, 296 (2009). doi:10.1038/nature07644 Medline

15. G. Kinoda *et al.*, Direct determination of localized impurity levels located in the blocking layers of $Bi_2Sr_2CaCu_2O_y$ using scanning tunneling microscopy/spectroscopy. *Phys. Rev. B* **71**, 020502 (2005). doi:10.1103/PhysRevB.71.020502

16. G. Kinoda, T. Hasegawa, Observations of electronic inhomogeneity in heavily Pb-doped $Bi_2Sr_2CaCu_2O_y$ single crystals by scanning tunneling microscopy. *Phys. Rev. B* **67**, 224509 (2003). doi:10.1103/PhysRevB.67.224509

17. M. Presland, J. Tallon, R. Buckley, R. Liu, N. Flower, General trends in oxygen stoichiometry effects on T_c in Bi and Tl superconductors. *Physica C* **176**, 95 (1991). doi:10.1016/0921-4534(91)90700-9

18. T. S. Nunner, B. M. Andersen, A. Melikyan, P. J. Hirschfeld, Dopant-modulated pair interaction in cuprate superconductors. *Phys. Rev. Lett.* **95**, 177003 (2005). doi:10.1103/PhysRevLett.95.177003 Medline

19. W. Chen, M. Gabay, P. J. Hirschfeld, Doping dependence of gap inhomogeneities at $Bi_2Sr_2CaCu_2O_{8+\delta}$ surfaces. *New J. Phys.* **14**, 033004 (2012). doi:10.1088/1367-2630/14/3/033004

20. S. Zhou, H. Ding, Z. Wang, Correlating off-stoichiometric doping and nanoscale electronic inhomogeneity in the high-T_c superconductor $Bi_2Sr_2CaCu_2O_{8+\delta}$. *Phys. Rev. Lett.* **98**, 076401 (2007). doi:10.1103/PhysRevLett.98.076401 Medline

21. D. B. Mitzi, L. W. Lombardo, A. Kapitulnik, S. S. Laderman, R. D. Jacowitz, Growth and properties of oxygen- and ion-doped $Bi_2Sr_2CaCu_2O_{8+\delta}$ single crystals. *Phys. Rev. B Condens. Matter* **41**, 6564 (1990). doi:10.1103/PhysRevB.41.6564 Medline

22. J. G. Bednorz, K. A. Müller, Possible high T_c superconductivity in the Ba-La-Cu-O system. *Zeitschrift für Physik B* **64**, 189 (1986). doi:10.1007/BF01303701

23. D. Zech *et al.*, Site-selective oxygen isotope effect in optimally doped $YBa_2Cu_3O_{6+x}$. *Nature* **371**, 681 (1994). doi:10.1038/371681a0

24. Y. Ohta, T. Tohyama, S. Maekawa, Apex oxygen and critical temperature in copper oxide superconductors: Universal correlation with the stability of local singlets. *Phys. Rev. B Condens. Matter* **43**, 2968 (1991). doi:10.1103/PhysRevB.43.2968 Medline

25. E. Pavarini, I. Dasgupta, T. Saha-Dasgupta, O. Jepsen, O. K. Andersen, Band-structure trend in hole-doped cuprates and correlation with T_{cmax}. *Phys. Rev. Lett.* **87**, 047003 (2001). doi:10.1103/PhysRevLett.87.047003 Medline

26. J. E. Hoffman *et al.*, A four unit cell periodic pattern of quasi-particle states surrounding vortex cores in $Bi_2Sr_2CaCu_2O_{8+\delta}$. *Science* **295**, 466 (2002). doi:10.1126/science.1066974 Medline

27. C. V. Parker *et al.*, Fluctuating stripes at the onset of the pseudogap in the high-T_c superconductor $Bi_2Sr_2CaCu_2O_{8+x}$. *Nature* **468**, 677 (2010). doi:10.1038/nature09597 Medline

28. Y. Kohsaka *et al.*, How Cooper pairs vanish approaching the Mott insulator in $Bi_2Sr_2CaCu_2O_{8+\delta}$. *Nature* **454**, 1072 (2008). doi:10.1038/nature07243 Medline

29. J. E. Hoffman *et al.*, Imaging quasiparticle interference in $Bi_2Sr_2CaCu_2O_{8+\delta}$. *Science* **297**, 1148 (2002). doi:10.1126/science.1072640 Medline

30. T. Hanaguri *et al.*, Quasiparticle interference and superconducting gap in $Ca_{2-x}Na_xCuO_2Cl_2$. *Nat. Phys.* **3**, 865 (2007). doi:10.1038/nphys753

31. E. Berg, D. Orgad, S. Kivelson, Route to high-temperature superconductivity in composite systems. *Phys. Rev. B* **78**, 094509 (2008). doi:10.1103/PhysRevB.78.094509

32. L. Goren, E. Altman, Enhancement of the critical temperature in cuprate superconductors by inhomogeneous doping. *Phys. Rev. B* **84**, 094508 (2011). doi:10.1103/PhysRevB.84.094508

33. T. Cren *et al.*, Influence of disorder on the local density of states in high-T_c superconducting thin films. *Phys. Rev. Lett.* **84**, 147 (2000). doi:10.1103/PhysRevLett.84.147 Medline

34. C. Howald, P. Fournier, A. Kapitulnik, Inherent inhomogeneities in tunneling spectra of $Bi_2Sr_2CaCu_2O_{8+x}$ crystals in the superconducting state. *Phys. Rev. B* **64**, 100504 (2001). doi:10.1103/PhysRevB.64.100504

35. Q.-H. Wang, J. Han, D.-H. Lee, Pairing near the Mott insulating limit. *Phys. Rev. B* **65**, 054501 (2001). doi:10.1103/PhysRevB.65.054501

36. Z. Wang, J. Engelbrecht, S. Wang, H. Ding, S. Pan, Inhomogeneous d-wave superconducting state of a doped Mott insulator. *Phys. Rev. B* **65**, 064509 (2002). doi:10.1103/PhysRevB.65.064509

37. P. Richard *et al.*, Nature of oxygen dopant-induced states in high-temperature $Bi_2Sr_2CaCu_2O_{8+x}$ superconductors: A photoemission investigation. *Phys. Rev. B* **74**, 094512 (2006). doi:10.1103/PhysRevB.74.094512

38. C. Howald, H. Eisaki, N. Kaneko, A. Kapitulnik, Coexistence of periodic modulation of quasiparticle states and superconductivity in $Bi_2Sr_2CaCu_2O_{8+\delta}$. *Proc. Natl. Acad. Sci. U.S.A.* **100**, 9705 (2003). doi:10.1073/pnas.1233768100 Medline

39. A. Mesaros *et al.*, Topological defects coupling smectic modulations to intra-unit-cell nematicity in cuprates. *Science* **333**, 426 (2011). doi:10.1126/science.1201082 Medline

40. W. D. Wise *et al.*, Charge-density-wave origin of cuprate checkerboard visualized by scanning tunnelling microscopy. *Nat. Phys.* **4**, 696 (2008). doi:10.1038/nphys1021

41. M. Boyer, thesis, Massachusetts Institute of Technology, Cambridge, MA (2008).

42. J.-H. Ma *et al.*, Coexistence of competing orders with two energy gaps in real and momentum space in the high temperature superconductor $Bi_2Sr_{2-x}La_xCuO_{6+\delta}$. *Phys. Rev. Lett.* **101**, 207002 (2008). doi:10.1103/PhysRevLett.101.207002 Medline

43. M. J. Lawler *et al.*, Intra-unit-cell electronic nematicity of the high-T_c copper-oxide pseudogap states. *Nature* **466**, 347 (2010). doi:10.1038/nature09169 Medline

44. E. W. Hudson, S.-H. Pan, A. K. Gupta, K.-W. Ng, J. C. Davis, Atomic-scale quasi-particle scattering resonances in $Bi_2Sr_2CaCu_2O_{8+\delta}$. *Science* **285**, 88 (1999). doi:10.1126/science.285.5424.88 Medline

45. S.-H. Pan *et al.*, Imaging the effects of individual zinc impurity atoms on superconductivity in $Bi_2Sr_2CaCu_2O_{8+\delta}$. *Nature* **403**, 746 (2000). doi:10.1038/35001534 Medline

46. E. W. Hudson *et al.*, Interplay of magnetism and high-T_c superconductivity at individual Ni impurity atoms in $Bi_2Sr_2CaCu_2O_{8+\delta}$. *Nature* **411**, 920 (2001). doi:10.1038/35082019 Medline

47. E. W. Hudson *et al.*, STM study of novel resonances in $Bi_2Sr_2CaCu_2O_{8+\delta}$. *Physica B* **329-333**, 1365 (2003). doi:10.1016/S0921-4526(02)02238-X

48. B. Koopman *et al.*, Scanning tunneling microscopy of Fe doped $Bi_2Sr_2CaCu_2O_{8+x}$. *Bull. Am. Phys. Soc.* **57**, H37.6 (2012).

49. H. Eisaki *et al.*, Effect of chemical inhomogeneity in bismuth-based copper oxide superconductors. *Phys. Rev. B* **69**, 064512 (2004). doi:10.1103/PhysRevB.69.064512

50. J. W. Alldredge *et al.*, Evolution of the electronic excitation spectrum with strongly diminishing hole density in superconducting $Bi_2Sr_2CaCu_2O_{8+\delta}$. *Nat. Phys.* **4**, 319 (2008). doi:10.1038/nphys917

51. J. Alldredge, K. Fujita, H. Eisaki, S. Uchida, K. McElroy, Three-component electronic structure of the cuprates derived from spectroscopic-imaging scanning tunneling microscopy. *Phys. Rev. B* **85**, 174501 (2012). doi:10.1103/PhysRevB.85.174501

52. S.-H. Pan *et al.*, STM studies of the electronic structure of vortex cores in $Bi_2Sr_2CaCu_2O_{8+\delta}$. *Phys. Rev. Lett.* **85**, 1536 (2000). doi:10.1103/PhysRevLett.85.1536 Medline